Physics of Fluids

RESEARCH ARTICLE | DECEMBER 18 2023

How do crosswinds from two turbulent generators affect the aerodynamic loads of running trains at tunnel entrances?

Huan Yue (岳欢) ; Jian Wang (王剑) ; E Deng (邓锷) ; Yi-Qing Ni (倪一清) ;
Wei-Chao Yang (杨伟超); Xin-Yuan Liu (刘新源) ; Cheuk-Man Tsang (曾卓文)

Physics of Fluids 35, 125137 (2023)
https://doi.org/10.1063/5.0177331

How do crosswinds from two turbulent generators affect the aerodynamic loads of running trains at tunnel entrances?

Cite as: Phys. Fluids **35**, 125137 (2023); doi: 10.1063/5.0177331
Submitted: 21 September 2023 · Accepted: 28 November 2023 ·
Published Online: 18 December 2023

Huan Yue (岳欢),[1,2] Jian Wang (王剑),[3] E Deng (邓锷),[1,2,a)] Yi-Qing Ni (倪一清),[1,2] Wei-Chao Yang (杨伟超),[3,4] Xin-Yuan Liu (刘新源),[1,2] and Cheuk-Man Tsang (曾卓文)[2]

AFFILIATIONS

[1]National Rail Transit Electrification and Automation Engineering Technology Research Center (Hong Kong Branch), Hong Kong, China
[2]Department of Civil and Environmental Engineering, The Hong Kong Polytechnic University, Hong Kong, China
[3]School of Civil Engineering, Central South University, Changsha, China
[4]National Engineering Research Center of High-speed Railway Construction Technology, Changsha, China

[a)]**Author to whom correspondence should be addressed:** early.deng@polyu.edu.hk

ABSTRACT

In order to investigate the effect of natural turbulent crosswinds on the aerodynamic loads of a high-speed train (HST) running through a tunnel entrance of high-speed railways, the new contribution is that the changing law of the HST's aerodynamic loads under the incoming turbulence with actual turbulence integral scale is revealed when the HST running in tunnel-flat ground-tunnel scenes, based on two types of turbulence generators with size scaled up by 8 times. The train surface pressure coefficients of the numerical model are compared with the corresponding results of wind tunnel experiments to verify the computational fluid dynamics method. The primary results show that the incoming turbulent flow generated by the spire is consistent with the characteristics of the measured wind. The peak aerodynamic load coefficients of the head carriage increase 1.12–1.5 and 1.06–2.0 times, respectively, under the incoming turbulent flow by the spire and fence, compared to the incoming flow of 11.50 m/s.

I. INTRODUCTION

With the extensive building of high-speed railway tunnels in China, infrastructure switching scenarios, such as tunnel-flat ground tunnel (TFT), are always considered in the operation of high-speed trains (HSTs). The HSTs' aerodynamic loads will suddenly change if HSTs encounter the crosswind at a tunnel entrance,[1–3] causing a significant threat to the HSTs' operational safety. The crosswinds at the entrance of mountain tunnels are often incoming turbulent flow with complex fluctuating components.[4] Turbulent characteristics of the incoming flow have an important influence on the HSTs' operational safety.[5–7] Theoretical derivation based on an empirical formula, wind tunnel testing, and numerical simulation are the three main techniques used to simulate turbulent wind.[8–12] Niu *et al.*[6] varied the incoming turbulent flow by adjusting the spires distance based on wind tunnel experiment. They also compared the aerodynamic coefficients and turbulence characteristics of the HST under turbulent incoming flow. In this study, by adjusting the size, spacing, and distance of the turbulence generator from the high-speed railroad line, incoming turbulent flow matching the actual turbulence integration scale are generated. Compared with the traditional wind tunnel and empirical formulas, the method is an economical choice, avoids the scale effect of wind tunnel experiments, and the simulated incoming turbulent flow is more consistent with the measured wind.

Crosswind has a significant effect on the operational safety of high-speed trains.[13–16] There is a potential risk associated with abrupt fluctuations in aerodynamic forces of high-speed trains under crosswinds. Based on the Lattice Boltzmann method (LBM), Masoud and Mohammad[17] investigated the law of the influence of fences on the strength of airflow over a high-speed train. The results show that crosswind has a significant effect on the aerodynamic loads of high-speed trains. The fence greatly reduces the wind speed above the high-speed train. Masoud and Mohammad[18] combined the LBM and multi-objective genetic algorithm to study the aerodynamics of wind protection devices for high-speed railroads and to optimize their shapes.

Based on field test and numerical simulations, Yang *et al.*[3] investigated the aerodynamic characteristics of the high-speed train at the tunnel-bridge section under natural wind. The results show that turbulent crosswinds cause sudden and continuous fluctuations in aerodynamic loads on high-speed trains.

The new contribution is that the changing law of the HST's aerodynamic loads (i.e., the lateral load, the lift load, the rolling moment, the yawing moment, and the nodding moment) under the incoming turbulence with actual turbulence integral scale is revealed when the HST running in the TFT scenes, based on two types of turbulence generators with size scaled up by 8 times. First, the wind field's characteristics are analyzed by the field measurement at the TFT scene. Then, combined with Fluent, a 3D air-HST-tunnel-flat ground-spire/fence CFD model is established. Finally, the HST's aerodynamic loads in the whole process of the TFT scene operation is analyzed under the incoming turbulent flow, and the mechanism of aerodynamic load changes is also revealed by wind speed, spectrum, and turbulence statistics.

II. FIELD TEST

A. Field test overview

Two 3D ultrasonic anemometers were positioned at the tunnel entrance for long-term sampling. These devices were used to obtain the measurements reported below, which in turn formed the basis of the turbulence generator methods used later in Sec. III for the incoming turbulent flow of the Improved Delayed Detached Eddy Simulation (IDDES).

From March to September 2021, a typical TFT site in Changsha, Hunan Province, China, was continuously sampled. Figure 1 shows the diagram of the field test. Two 3D ultrasonic anemometers (32 Hz) are located at measurement points No. 1 and No. 2 on the west side of the high-speed railway. The distance between No. 1 and No. 2 is 0.26*L* (the length (*L*) of the HST is 76.65 m).

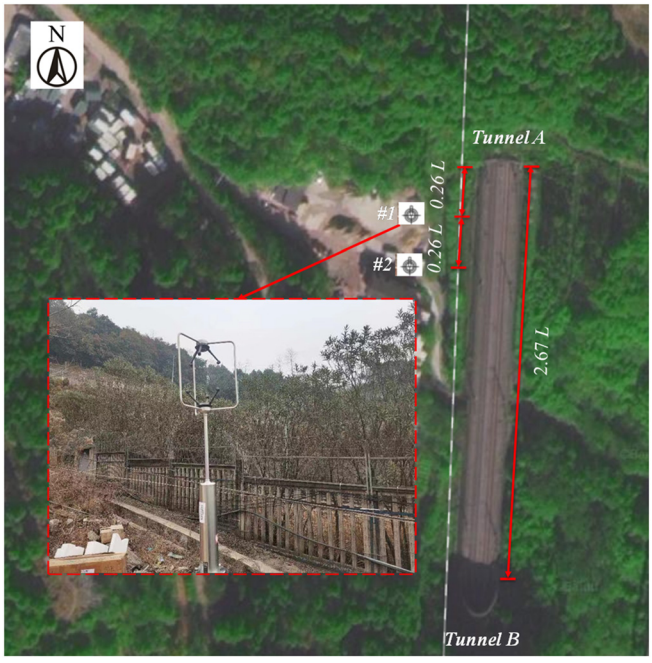

FIG. 1. The field test diagram of the TFT.

B. Mean wind velocity and direction

The HST's running time in the TTF scenario is 3 s or less. Therefore, the wind velocity data collected during the 4 h continuous period with the strongest wind on site are segmented by a 3 s time interval. Radar maps are used to display the sample's 4 h mean wind speed ($\overline{U}$) and direction ($\overline{\theta}$) (Fig. 2). The equations are used to obtain $\overline{U}$ and direction $\overline{\theta}$ for each sample,

$$\overline{U} = \frac{1}{n}\sum_{i=1}^{n}\sqrt{U_{Hi}^2 + U_{wi}^2}, \tag{1}$$

$$\overline{\theta} = \frac{1}{n}\sum_{i=1}^{n}\theta_i. \tag{2}$$

Figure 2 shows that as the wind velocity increases, the mean wind direction of the Nos. 1 and 2 measuring points is perpendicular to the direction of the HST operation, and the majority of wind angles are 270° (Rotated clockwise from due north, the wind direction is from 0° to 360°). The sample's greatest mean wind velocity is 14.1 and 13.9 m/s at Nos. 1 and No. 2, respectively. Both Nos. 1 and No. 2 measuring point's high wind velocity segments primarily fall within the 10–14 and 9–14 m/s ranges.

C. Turbulence intensity

The *Z* direction is specified as the *u* component (U_H and U_w represent the horizontal wind velocity and the vertical wind velocity). The following equations determine the turbulence intensity (I_u) on the Z (*u*). Figure 3 displays the turbulence intensity's scatterplot.

$$\sigma_u = \sqrt{\frac{\sum_{i=1}^{n}(U_{ui} - \overline{U_u})^2}{n-1}}, \tag{3}$$

$$I_u = \frac{\sigma_u}{\overline{U}}, \tag{4}$$

where U_{ui} represents wind velocity's *u* component for each sample.

Turbulence intensity refers to the velocity change magnitude of the incoming turbulent flow, which is important for the study of

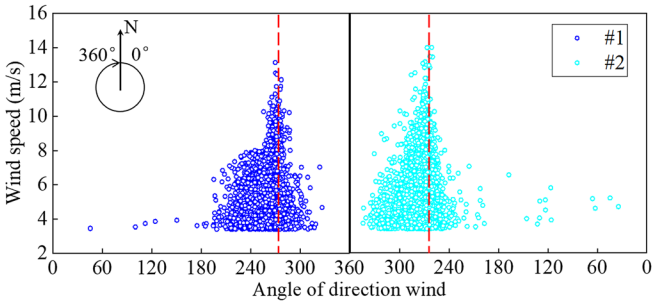

FIG. 2. Wind speed-direction.

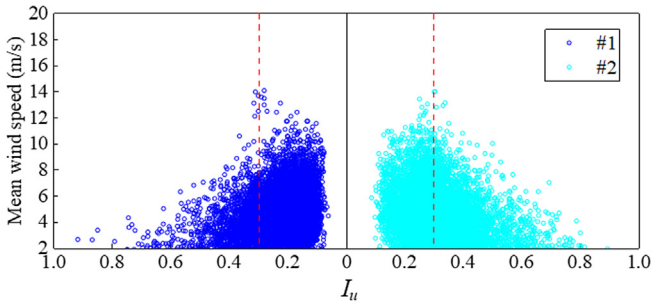

FIG. 3. Turbulence intensity scatterplot.

vibration and aerodynamic loads fluctuation of the HST. When the wind speed is less than 12 m/s, as the wind speed increases, the variance range of turbulence intensity gradually decreases. The turbulence intensity of No. 1 tends to be around 0.2, while the turbulence intensity of No. 2 is larger and tends to be near the range of 0.3. When the wind velocity exceeds 12 m/s, Fig. 3 shows that the turbulence intensity tends to stabilize. The turbulence intensity of both No. 1 and No. 2 tends to be 0.3. The incoming flow with high wind speed significantly influences the HST's aerodynamic loads. Therefore, the turbulence intensity (0.3) of the incoming flow of 14 m/s is taken as the typical turbulence intensity of the simulation.

III. CFD modeling

A. IDDES

IDDES is a hybrid LES/RANS method, which solves the near-wall flow of the turbulence generator and the HST by RANS, while LES is used for solving the rest of the model. IDDES permits a switch from RANS to LES. The model couples the RANS and LES approaches by blending their respective length scales for the eddy viscosity. For the near-wall flow, Fluent utilizes a revised SST k-ω model, and readers may refer to Shur *et al.*[19] and Gritskevich *et al.*[20] for a comprehensive explanation of the model equations.

B. Geometry and solution domain

Figure 4 displays the geometric solution domain of a model comprising a HST-tunnel-flat ground-tunnel-spire/fence model. The CRH380B HST is divided into three carriages (i.e., head, middle and rear carriage). The HST's width (W) and height (H) are 3.625 and 3.89 m, respectively. Neglecting the bogie, the distance between the ground and the HST bottom is 0.051H. The mountain has a slope and the height is 5.34H, and the tunnel portal is of the cap oblique cutting type. The turbulence generator, whether it be the spire or fence, with the same blocking rate, is positioned 2.76W away from the railway line to simulate the incoming turbulent flow at the tunnel entrance. The wind tunnel laboratory' spire is enlarged by eight times its original size. Figure 4(a) depicts the size of the spire. A total of 19 spires are arranged along the high-speed railway, and the flat ground section's blocking rate is 7.1%. The width of the upper and lower part of the spire is 0.0015 and 0.05L, respectively, and the interval between the two spires is 0.05L. The height and width are 5.08H and 0.71W, respectively.[6] Figure 4(b) shows the size of the fence. The width of the square hole and the rib are 0.05 and 0.014L. The tunnel dimensions

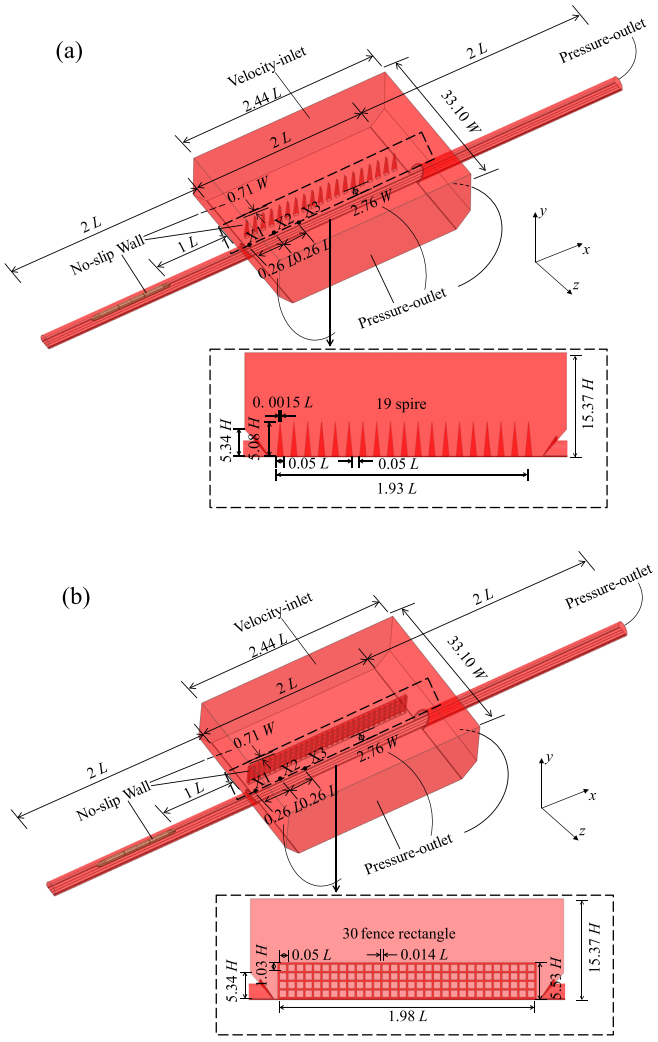

FIG. 4. The geometric solution domain: (a) spire and (b) fence.

are 2L, 3.48W, and 2.33H, respectively, and it has a clearance area of 100 m^2.[21] The interval between the two operating lines is 1.38W. The operating line close to the velocity-inlet is the windward side (WWS) line, and the opposite is the leeward side (LWS) line. On the WWS line, 0, 0.26, and 0.52L, respectively, from the entrance of tunnel A, at a height of 2.5 m, three measuring points (X1, X2, and X3) are placed as the center of the three directions.

C. Initial and boundary conditions

The velocity-inlet is utilized in the turbulence generator's WWS. The surfaces of the spire, HST, ground, tunnel wall, and mountain wall are set to no-slip walls. The tunnel outlet is a pressure outlet, comprising of the top surface and the remaining atmospheric outlet. The CFD model is initialized from the velocity-inlet with an initial wind velocity of 20 m/s. The HST is placed initially within tunnel A with the head carriage positioned 1L from the entrance to tunnel A.

TABLE I. Calculation cases are considered in this study.

Case	HST movement	Inlet velocity (m/s)	Turbulence generator
C1	Static	20	Spire
C2	Static	20	Fence
C3	Dynamic	11.50	Without
C4	Dynamic	14.46	Without
C5	Dynamic	20	Spire
C6	Dynamic	20	Fence

D. The cases considered

As shown in Table I, six cases are considered in the study, which can be divided into two conditions: static models (C1 and C2) where the HST is stationary to study the incoming turbulent flow of the TFT. In the absence of the HST, and these structures are meshed to resolve the flow around them. The C3–C6 are used to study the aerodynamic forces of moving HSTs under the incoming turbulent flow generated by spires or fences. The wind velocity of the C3 and C4 is 11.50 and 14.46 m/s, respectively, and there is no dynamic model of the turbulence generator on the WWS line. The wind velocity of the C5 and C6 is 20 m/s, and the turbulence generators on the WWS are the spire and the fence.

E. Computational mesh

Figure 5 depicts the mesh of the HST-tunnel-flat ground-tunnel-spire model. The static model has a static mesh area when there is no HST movement (C1 and C2). With the absence of the HST, these structures are meshed to resolve the flow around them. As the HST moves, the mesh comprises dynamic mesh (A) and static mesh (B), and the HST is driven by sliding mesh technology. The flow field information is interlinked by establishing an interface between the dynamic and static mesh, ensuring the transient calculation of the flow field.

The mesh size ranges from 0.001 to 1 m, and the turbulence generator's surface has a mesh size of 0.001–0.1m. There are ten levels of boundary layer setup. The mesh resolution is enhanced by limiting the mesh size within 0.1 m surrounding the turbulence generator.

The HST and its surrounding air domain are located in the A_0 region of the dynamic mesh area [see Fig. 5(b)]. The size of the HST body wall is approximately 1–10 mm, with ten boundary layers setup on the HST. The first layer is estimated to have a thickness of 0.02–1 mm ($y^+ \approx 1$), while a 0.33L refined area is situated at the rear of the HST for more precise simulation of the HST wake vortex. With a mesh size of 0.1 m, structured meshes are used to separate the A_1 and A_2 areas. During the movement, the mesh layer at the back end of A_1 near the boundary is stretched. In addition, if the mesh layer is larger than the set size, it is automatically split into two layers, with the mesh layer adjacent to the boundary of the A_2 front end being compressed. Then, if the mesh layer is smaller than the set size, it is automatically merged with the adjacent mesh layer. Both ends of the mesh are set as static surfaces, while the remaining mesh types in the dynamic mesh region are set to rigid. The forward motion of the HST model can be simulated by assigning a velocity value to the rigid body.

F. Solution procedure, discretization and convergence

In the IDDES method, the RANS model is employed to simulate the near-wall flow of the HST and spire (fence) surface. The model

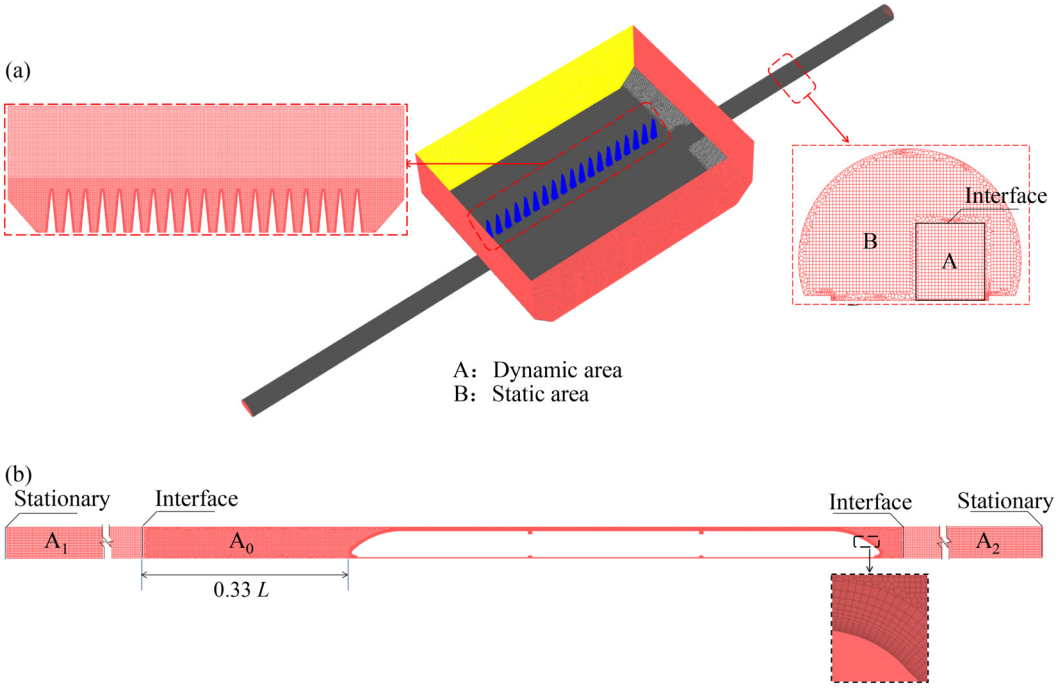

FIG. 5. Computational mesh: (a) overall mesh and (b) dynamic mesh.

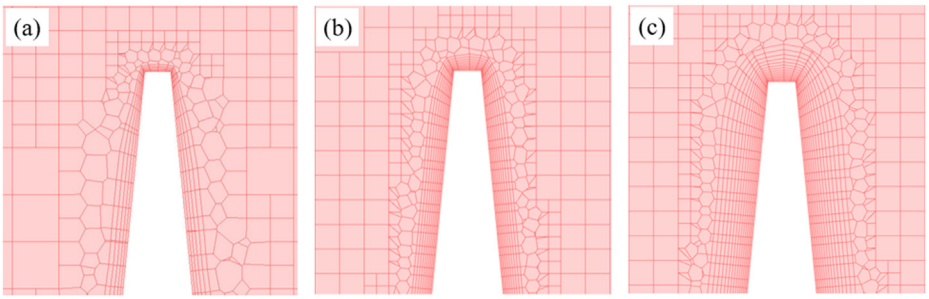

FIG. 6. Different mesh resolutions mesh: (a) spire-C, (b) spire-M, and (c) spire-F.

possesses the capacity to simulate complex flow. Regarding the near-wall region, the IDDES incorporates 10 boundary layers and applies near-wall treatment to resolve the complex flow near the wall. The y+ values typically range from unity or less.[22]

A high-resolution total variation diminishing time discretization scheme is used to solve the numerical models.[23] Due to the complexity of the simulation, the boundary layer element type is more complex and has a large aspect ratio of the curved mesh. In the transient solution, the double time step is used. By adding a fictitious time step to the calculation, the unsteady problem becomes a pseudo-stationary problem and the implicit convergence is accelerated. The total simulation time is 5 s, the total number of computational steps is 50 000, the physical time step is 10^{-4} s, and the iterations' numbers are 50 steps. During the model calculation, the residuals converge within 10^{-6} and the model convergence is good. Therefore, the double time step method improves the stability of the calculation, allows a larger physical time step and improves the computational efficiency. All CFD models are calculated using 144 cores in Wuxi, Jiangsu Province, China. The calculation time for C1 and C2 conditions is approximately 5 days, and the calculation time for C3–C6 conditions is approximately 8 days.

G. Mesh sensitivity study

Combined with the high-resolution scheme adopted by Thornber and Drikakis,[24] the mesh sensitivity of this research model is investigated using the HST tunnel-flat-tunnel-spire CFD model as an example. The mesh size and boundary layer number of the spire surface are refined. The mesh numbers are 25×10^6 (Spire-C), 45×10^6 (Spire-M), and 55×10^6 (Spire-F), respectively (Fig. 6). The velocity input of C1 is kept 20 m/s to monitor the wind velocity of X1 [Fig. 7(a)] and X2 [Fig. 8(a)]. Then, 10^{-4} and 5×10^{-5} s are used for comparison and the wind velocity of X1 and X2 is monitored to assess the sensitivity of the time step [Figs. 7(b) and 8(b)].

The information found in Figs. 7 and 8 is as follows: the maximum difference between the wind velocity of the Spire-M mesh and the corresponding value of the Spire-F mesh is less than 5%. A 20% deviation exists between the calculation results of the Spire-C and Spire-F mesh. The 45×10^6 (Spire-M) mesh model can obtain stable and accurate results. When the time steps are 10^{-4} and 5×10^{-5} s, the deviation is not more than 0.5%. The simulation results of 45×10^6 (Spire-M) are reliable. Therefore, the 45×10^6 (Spire-M) mesh model is used for the study.

H. CFD validation

The surface pressure of the HST under crosswind was tested using the dynamic HST with a scale ratio of 1:16.8 at the high-speed railway wind tunnel laboratory of Central South University (Fig. 9).[6] During the experiment, the HST ($V = 6$ m/s) runs on the WWS under the incoming flow ($U = 8$ m/s). The pressure value filtered by Eq. (5) should be dimensionless.

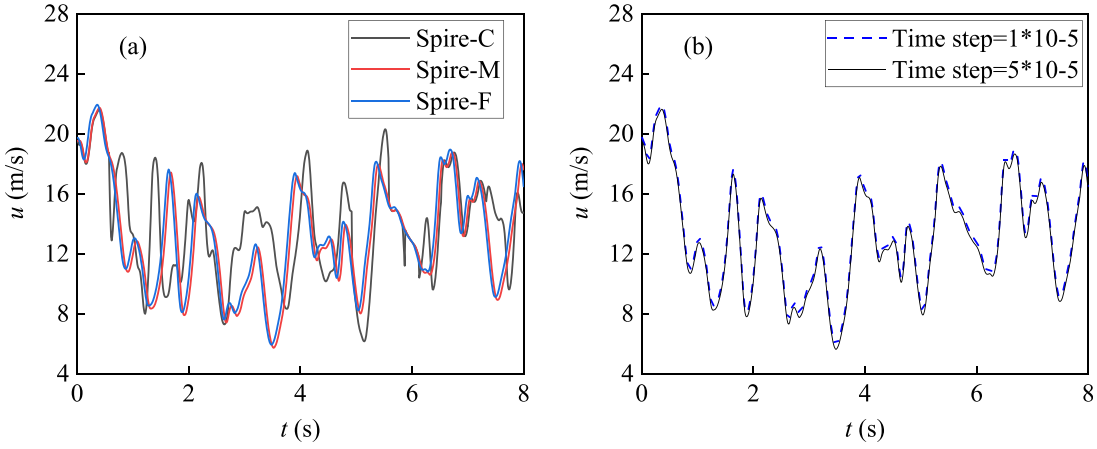

FIG. 7. The wind velocity of X1: (a) different mesh resolution conditions and (b) different time steps.

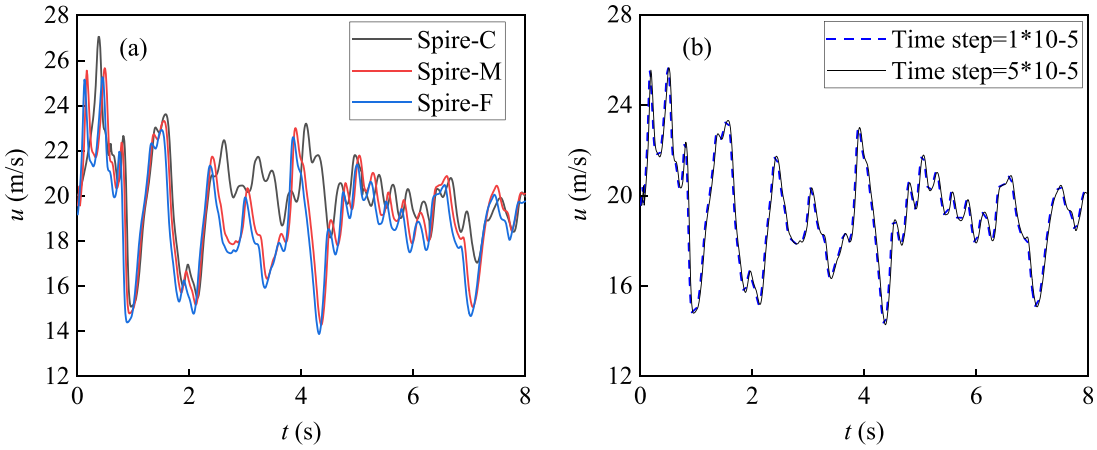

FIG. 8. The wind velocity of X2: (a) different mesh resolution conditions and (b) different time steps.

$$C_p = \frac{P_i - P_0}{\frac{1}{2}\rho U^2}, \tag{5}$$

where ρ is the air density, and P_0 represents the pressure inside the wind tunnel.

The results of eight replicate experiments are analyzed to determine the uncertainty of the experiment. Figure 10 shows the results of the experiment. The mean value of the surface pressure coefficient of the eight experiments is the final result, and the uncertainty of the experiment is calculated. The time history of the HST surface pressure in eight experiments is similar, and the experimental results are stable. The calculated experimental uncertainty is 0.005.

As shown in Fig. 9, the mesh size of the whole computational domain is 0.5–10 mm, the surface size of the HST is 0.5–1 mm, and there are 10 boundary layers on the HST surface. Moreover, 45×10^6 and 55×10^6 are set using the high-resolution method to analyze the difference between CFD and test. Figure 11 shows the HST surface pressure of CFD and test. In addition, based on the high-resolution mesh, the influence of the initial conditions [initial wind speed is 0 ($I_{U=0}$) and initial wind speed is 8 m/s ($I_{U=8}$)] on the numerical simulation results is discussed.

As shown in Fig. 11, the results of the associated wind tunnel tests are essentially in agreement with the time history of the HST surface pressure as determined by the high-resolution mesh calculation. The difference between the CFD and the test is mainly due to the surface

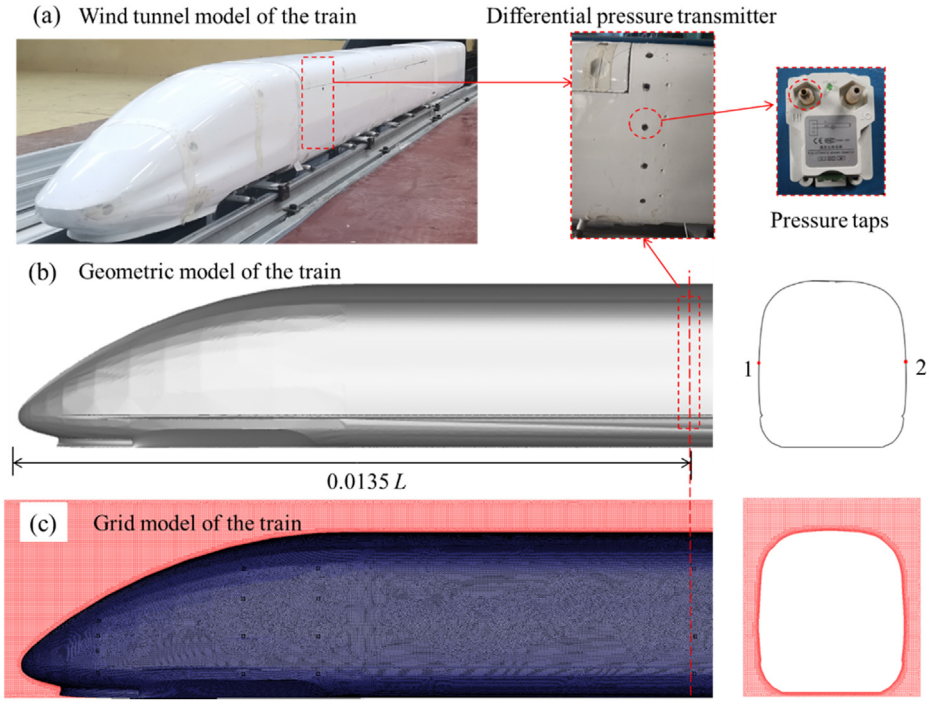

FIG. 9. TFT moving HST model wind tunnel test system:(a) wind tunnel model of the train, (b) geometric model of the train and (c) grid model of the train.

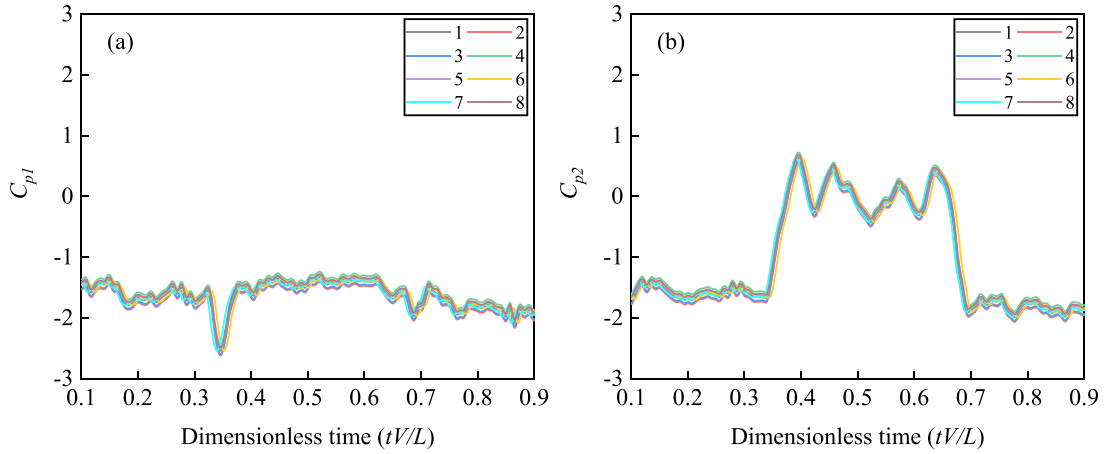

FIG. 10. Eight times the surface pressure of the HST: (a) No. 1 and (b) No. 2.

pressure of the body, which fluctuates strongly when the HST is running in the crosswind. The maximum difference between the measured pressure coefficient and the experimental value within 8%. The initialization conditions have little effect on the computational results, because when the HST leaves the tunnel, the wind field at the tunnel entrance has been calculated to be stable. Therefore, the mesh resolution has a major impact on the calculation accuracy. The IDDES-based high-resolution numerical simulation technique is reliable.

IV. RESULTS AND DISCUSSION

A. Wind field characteristics simulated by turbulence generator

1. Flow field simulated by turbulence generator

Turbulent kinetic energy (TKE) is the kinetic energy generated due to irregular turbulent flow in fluid motion, and it is an important index to study the airflow velocity decay pattern on the leeward side of the turbulence generator. Therefore, Figs. 12 and 13 show the averaged flow field and TKE of the C1 and C2, respectively ($U_0 = 20$ m/s).

TKE is defined as

$$k = \frac{1}{2}(\tilde{u}^2 + \tilde{v}^2 + \tilde{w}^2), \tag{6}$$

where $\tilde{u}$ $\tilde{v}$ $\tilde{w}$ stand for variable wind velocity's root mean square.

As shown in Fig. 12, the incoming flow will accelerate through the center of the two spires due to the canyon tube effect as the incoming flow passes the spire. The airflow generates a large wake region on the spire's LWS, along with turbulence and vortices. This flow pattern leads to pressure changes on the spire's LWS, resulting in large areas of negative pressure. The flow between the two spire regions can be disturbed by each other, resulting in locally accelerated flows. This interaction may cause instability in the airflow leading to local pressure changes and vortex generation. The flow pattern between the LWS of the spire and the space between the two spires differs markedly, and the wind speed on the WWS of the line fluctuates greatly. When the attenuation rate of downstream wind speed is large, that is, the downstream wind speed decreases rapidly after passing through the spire, which may lead to an increase in upstream wind speed. This is because the turbulence and eddies

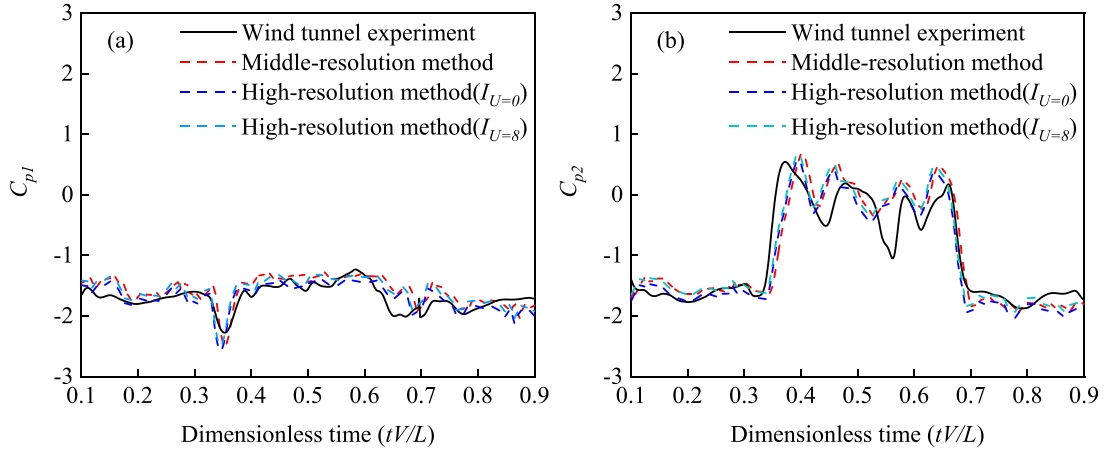

FIG. 11. Surface pressure of the HST of test and CFD: (a) No. 1 and (b) No. 2.

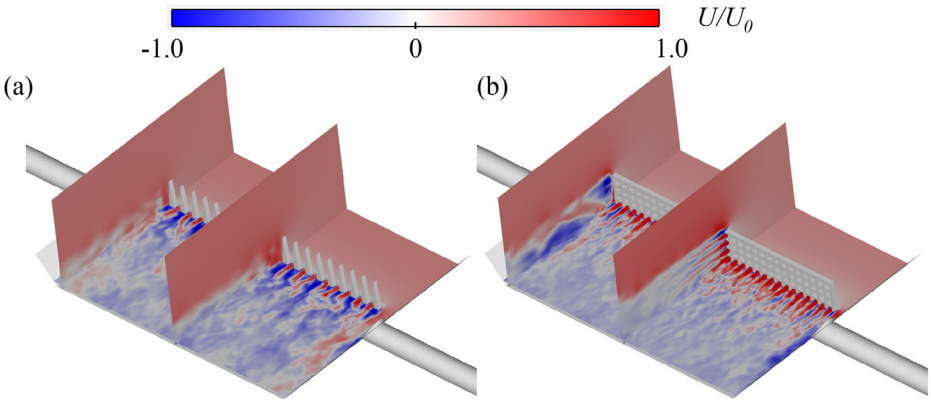

FIG. 12. Flow field of the TFT scene: (a) C1 and (b) C2.

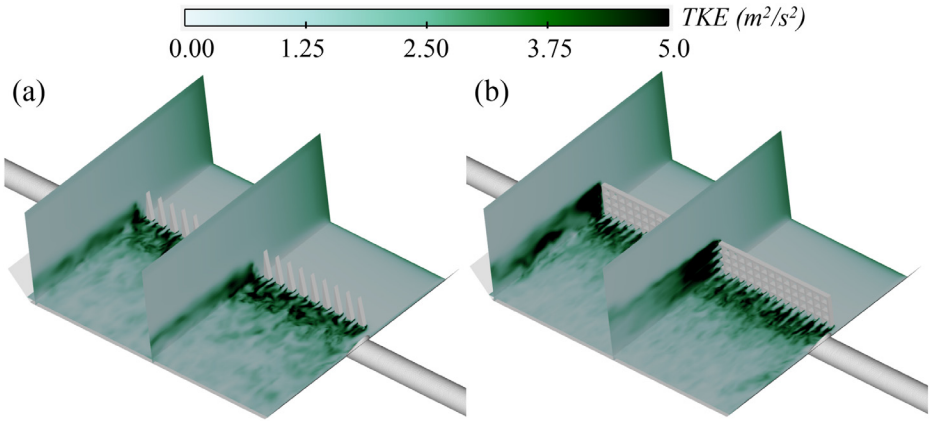

FIG. 13. TKE of the TFT scene: (a) C1 and (b) C2.

downstream have an effect on the upstream airflow, causing it to be accelerated. The attenuation rate of the incoming flow at the LWS of the fence is lower than that of the spire, so the wind speed along the WWS of the line is higher. The incoming flow, after passing through the fence, creates a low-speed region on the LWS of the tunnel portal [the blue area of the tunnel entrance in Fig. 12(b)], which is quite different from the actual measurement. The wind speed at the LWS of the spire increases with height. The wind speed at the LWS of the fence edges up with height.

As shown in Fig. 13, for C1 the incoming flow forms a strong TKE zone at the LWS of the gap between the two spires (particularly in the near-surface region). The TKE drops sharply between the spire and the LWS. Therefore, as shown in Fig. 13(a), the turbulence intensity of the LWS is large and varies rapidly. As shown in Fig. 13(b), in contrast to the spire, the incoming flow generates a wider range of strong TKE regions on the LWS of the fence, where the LWS of the spire experiences less attenuation of the wind velocity than the fence. Therefore, the wind speed along the LWS of the fence is higher than that of the spire. In the near ground region (2.5 m from the ground), as the TKE decays to a stable state, the spire and fence LWS have the same turbulence intensity.

2. Power spectral density (PSD) analysis

Figure 14 shows the power spectrum of the measured No. 1 and X2 simulated by C1 and C2. The peak PSD value of the C1 is 162 times that of C2. The peak PSD value difference between C1 and the measured is only 12%. Figure 14 shows that the C1 wind power spectrum matches the measured wind power spectrum more closely. According to the formula of wind power spectrum, the turbulence

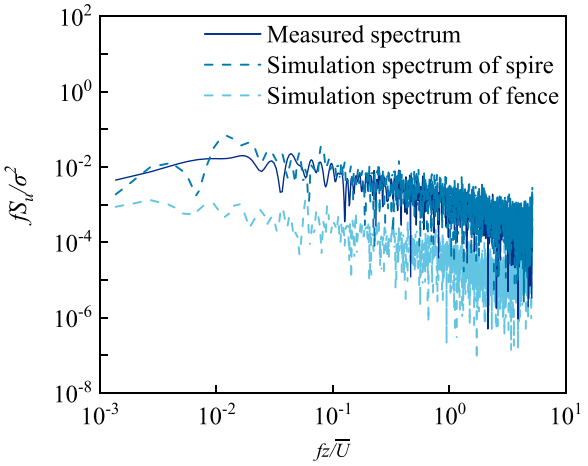

FIG. 14. Comparison of measured and simulated PSD curves.

integral scale can be calculated.[3] The wind power spectrum of C2 is not well matched. The turbulence integral scale of X2 as predicted by C1 is 49.3, which is similar to the measured value of 50.37 m. The measured value is far from the matching value of the C2 state simulation, which is 90.46 m. The reason for the difference between the simulated C2 results and the actual measurements in the PSD analysis is the difference between the turbulence pattern and the attenuation law of the airflow at the leeward side of the spires or fences and the actual turbulent.

B. HST's aerodynamic characteristics

1. HST's aerodynamic loads

The variation in wind speed causes the aerodynamic load to change. Figure 15 shows the five nonlinear aerodynamic forces of the HST to study the effect of the turbulent flow of the spire and fence on the aerodynamic load of the moving HST.

The nonlinear aerodynamic force of the HST was calculated using the unit surface pressure integral method,[3] and the dimensionless coefficients of the nonlinear aerodynamic forces were calculated using Eqs. (7) and (8). The lateral load coefficient C_z, the lift load coefficient C_y, the rolling moment coefficient C_{mx}, the yawing moment coefficient C_{my}, and the nodding moment coefficient C_{mz} (i.e., head C_z represents the lateral load coefficient of the head carriage). Table II shows the maximum peak values of the five aerodynamic loads of three HSTs' carriage. Table III calculates the standard deviation of the nonlinear aerodynamic force of three HSTs' carriage,

$$\begin{cases} C_i = F_i/(0.5\rho V_a^2 A), \\ C_{mi} = M_i/(0.5\rho V_a^2 A h), \end{cases} \tag{7}$$

$$V_a^2 = V_t^2 + u^2, \tag{8}$$

where ρ represents the density of air, where the value is 1.205 kg/m^3, and V_a represents the incoming and outgoing wind velocity relative to the moving HST (V_t).

Figure 15 and Tables II and III provide the following conclusions:

A HST's aerodynamic load coefficient changes dramatically when it enters and exits a tunnel, and the peak nonlinear aerodynamic force is higher. During periods of incoming flow, the HST's five nonlinear aerodynamic forces after the HST runs on the open line remain at the peak level and fluctuate stably. However, the HST's nonlinear aerodynamic force fluctuated greatly in the open section when the incoming turbulent flow generated by a turbulence generator. The aerodynamic load fluctuations and dynamic response caused by the incoming flow will first be reflected in the head carriage, which in turn will have an impact on the whole HST. The incoming flow will cause the head carriage to be subjected to larger lateral forces and rolling moments, the dynamic response indexes of the HST will increase accordingly, and the HST will be more prone to derailment. Therefore, the study of the aerodynamic loads of the head carriage is essential to ensure the stability and safety of the HST. Furthermore, the aerodynamic load of the HST fluctuates under incoming turbulent flow, and when the aerodynamic loads of the train attain the peak value, the HST's operational safety is most threatened. Therefore, the effect of incoming turbulent flow generated by spires and fences on the peak aerodynamic coefficients of the head carriage will be mainly focused to analyze in following.

For C_z [as shown in Fig. 15(a_1) and Tables II and III], the head carriage is subjected to the greatest lateral force impact relative to the center and rear carriage as the HST exits or enters the tunnel. When the HST is running on the open line, with the incoming flow of 11.50 m/s, the C_z peak value of the head carriage is 0.089 and the standard deviation is 0.040. Compared with the constant wind speed of 11.50 m/s, the peak Cz of the head carriage increases by 1.36 and 1.56 times, and the standard deviation of the Cz of the head carriage increases to 0.005 and 0.008, respectively, under the turbulent flow of the spire or the fence.

For C_y [as shown in Fig. 15(b_1) and Tables II and III], the head carriage is subjected to a downward force when the HST runs in a tunnel. Therefore, the head carriage's C_y is negative. When the HST runs under crosswind, it has an overall upward tendency, and the three carriages' C_y is positive. As the HST is pulling out of the tunnel under the incoming flow of 11.50 m/s, the peak C_y of the middle carriage is 0.061, and the standard deviation is 0.023. Under the incoming flow of 14.46 m/s, peak C_y increases by 1.26 times, and the standard deviation increases to 0.030. Under the turbulent flow, the peak C_y of the head carriage increases by 1.23 or 1.25 times, respectively, and the standard deviations are 0.019 and 0.020. When the HST runs completely on the flat ground line, the standard deviation of the C_y is 0.001 under the incoming flow. The C_y standard deviation of the middle carriage is 0.011 and 0.009 under the turbulent wind.

For C_{mx} [as shown in Fig. 15(c_1) and Tables II and III], under the turbulent flow, the three carriages' C_{mx} fluctuates sharply. When the HST leaves the tunnel, under the incoming flow of 11.50 m/s, the head carriage's peak C_{mx} is 0.002, and the standard deviation is 0. Under the incoming turbulent flow, the peak C_{mx} of the head carriage is 1.5 and 2 times that of the incoming flow of 11.50 m/s.

For C_{my} [as shown in Fig. 15(d_1) and Tables II and III], the head carriage's C_{my} fluctuates the most compared to the center and rear carriages. With the incoming flow of 11.50 m/s, the peak C_{my} is 0.172 and the standard deviation is 0.064. Under the turbulent flow of the spire or fence, the peak C_{my} of the head carriage is 1.46 and 1.59 times, and the standard deviations are 0.068 and 0.081. When the HST is running on the open line and the incoming flow of 11.50 m/s, the peak C_{my} of the head carriage is 0.140 and the standard deviation is 0.001. Under the turbulent wind of the spire or fence, the peak C_{my} of the head carriage increases by 1.46 and 1.06 times, and the standard deviations are 0.034 and 0.029.

For C_{mz} [as shown in Figs. 15(e_1) and Tables II and III], with a constant incoming wind speed of 11.50 m/s, the peak C_{mz} of the head carriage is 0.112. Under the turbulent wind of the spire or the fence, the peak C_{mz} of the head carriage is 1.12 and 1.32 times, respectively. When the HST is completely outside the tunnel, the C_{mz} standard deviations of the head carriage under the spire or the fence's turbulent flow are 0.020 and 0.010, respectively, which are 20 and 10 times higher than C_{mz} standard deviations within the incoming flow of 11.50 m/s.

Riding comfort is defined as the standard deviation of the rolling moment coefficient. A larger standard deviation of the rolling moment coefficient means that the rolling moment of the train carriages varies more, and the violent shaking of the carriages leads to a reduction in riding comfort. Ride comfort is greatly reduced when the HST is running under the turbulent flow of the spire and fence compared to the constant incoming flow.

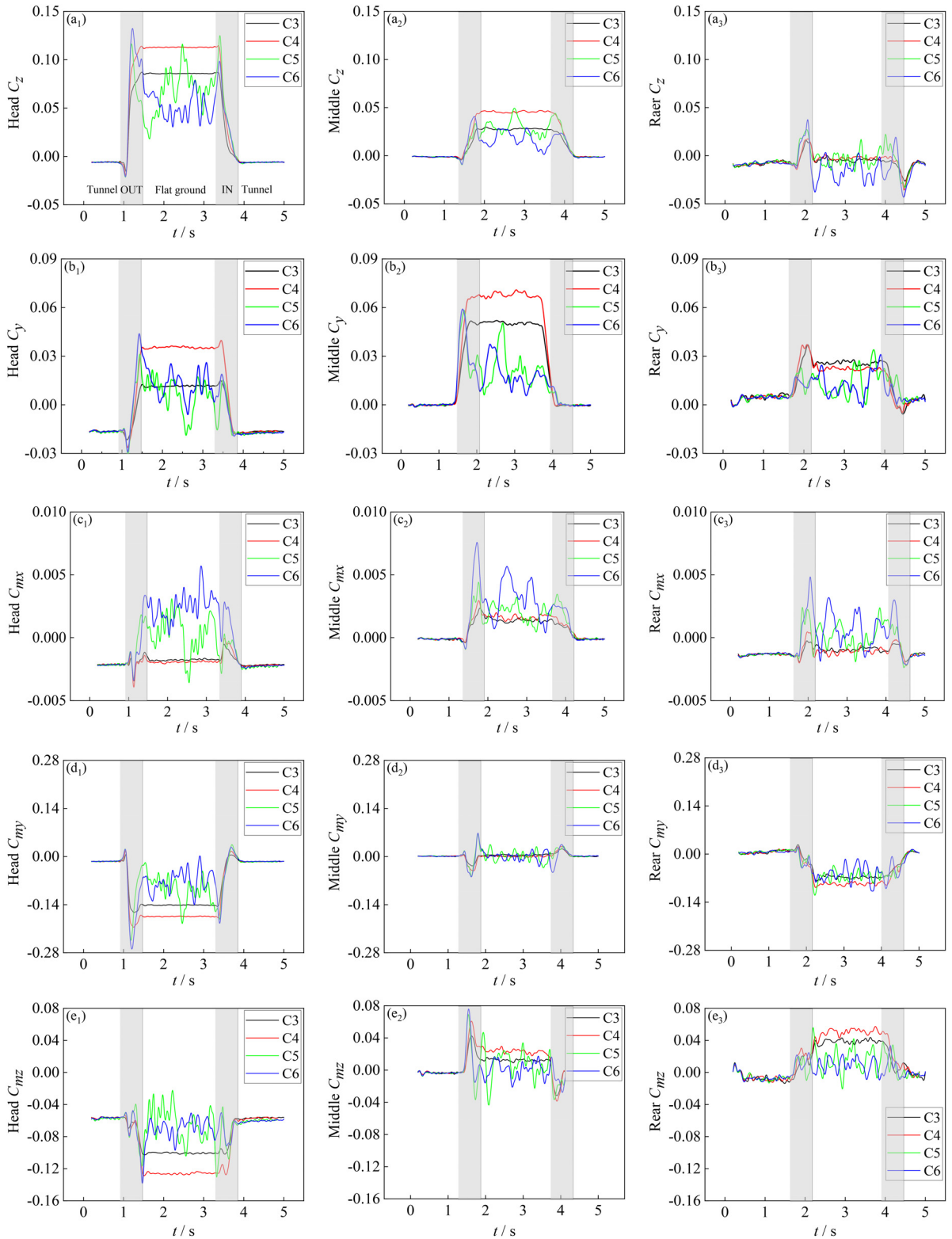

FIG. 15. Aerodynamic load coefficients: (a) C_z, (b) C_y, (c) C_{mx}, (d) C_{my}, and (e) C_{mz}.

TABLE II. The maximum value of the nonlinear aerodynamic force factor of the three carriages.

		OUT				Crosswind				IN			
	Carriage	C3	C4	C5	C6	C3	C4	C5	C6	C3	C4	C5	C6
Max C_Z	Head	0.089	0.117	0.121	0.139	0.088	0.115	0.119	0.080	0.088	0.115	0.128	0.101
	Middle	0.031	0.048	0.037	0.043	0.029	0.048	0.050	0.030	0.028	0.046	0.044	0.024
	Rear	0.020	0.023	0.031	0.041	−0.008	−0.005	−0.017	−0.033	−0.028	−0.037	−0.033	−0.045
Max C_y	Head	0.020	0.044	0.039	0.052	0.016	0.042	0.024	0.029	0.017	0.042	0.018	0.022
	Middle	0.061	0.077	0.075	0.076	0.057	0.074	0.055	0.043	0.052	0.069	0.027	0.023
	Rear	0.049	0.056	0.039	0.038	0.031	0.029	0.038	0.033	0.030	0.024	0.024	0.032
Max C_{mx}	Head	−0.002	−0.004	0.003	0.004	−0.002	−0.002	0.004	0.006	−0.002	−0.003	−0.003	−0.003
	Middle	0.003	0.017	0.051	0.015	0.002	0.002	0.003	0.006	0.001	0.002	0.003	0.003
	Rear	0.001	0.033	0.043	0.047	−0.001	−0.002	0.002	0.003	−0.002	−0.002	−0.002	−0.002
Max C_{my}	Head	−0.172	−0.213	−0.251	−0.273	−0.140	−0.177	−0.201	−0.149	−0.145	−0.178	−0.191	−0.202
	Middle	−0.015	−0.055	−0.026	−0.009	0.008	0.004	0.032	0.023	0.023	0.031	0.031	0.039
	Rear	−0.080	−0.023	−0.031	−0.004	−0.074	−0.096	−0.086	−0.110	−0.068	−0.092	−0.076	−0.099
Max C_{mz}	Head	−0.112	−0.138	−0.125	−0.145	−0.105	−0.131	−0.112	−0.101	−0.105	−0.131	−0.135	−0.094
	Middle	0.051	0.015	0.078	0.048	0.016	0.032	0.037	0.021	−0.034	−0.040	−0.041	−0.027
	Rear	0.043	0.047	0.056	0.023	0.044	0.058	0.049	0.026	0.040	0.053	0.039	0.015

In summary, under incoming flow, the maximum five nonlinear aerodynamic force coefficients of the HST are obtained when the HST exits the tunnel. When the velocity input is a constant wind speed, the nonlinear aerodynamic force coefficient of the HST after leaving the tunnel slightly fluctuate, which is often contrary to the actual situation.[25] The peak nonlinear aerodynamic force as the HST exits the tunnel is greater under the turbulent flow of the fence than that of the spire. However, when the HST runs on the open line, the nonlinear aerodynamic force of the HST fluctuates greatly under the turbulent flow of the spire. This is because the turbulent flow from the spire has a higher turbulence intensity on the WWS.

2. Transient vortex structure evolution

Figures 16–18 show the transient vortex structure. The contour surface of the eddy current structure in the diagram is created and colored with a dimensionless composite velocity ($Q = 3000$, $U_0 = 20$ m/s).

Figures 16–18 show the following:

TABLE III. The standard deviation of five nonlinear aerodynamic force coefficients for three carriages.

		OUT				Crosswind				IN			
	Carriage	C3	C4	C5	C6	C3	C4	C5	C6	C3	C4	C5	C6
σC_Z	Head	0.040	0.044	0.045	0.048	0.000	0.001	0.017	0.012	0.037	0.048	0.043	0.034
	Middle	0.014	0.021	0.015	0.015	0.001	0.001	0.008	0.008	0.012	0.019	0.017	0.010
	Rear	0.008	0.010	0.013	0.019	0.001	0.001	0.007	0.009	0.007	0.010	0.014	0.015
σC_y	Head	0.014	0.025	0.018	0.022	0.001	0.001	0.010	0.008	0.014	0.024	0.012	0.013
	Middle	0.023	0.030	0.019	0.020	0.001	0.002	0.011	0.009	0.020	0.027	0.009	0.008
	Rear	0.011	0.012	0.007	0.007	0.002	0.002	0.010	0.008	0.010	0.008	0.007	0.006
σC_{mx}	Head	0.000	0.001	0.002	0.002	0.000	0.000	0.002	0.002	0.001	0.001	0.001	0.002
	Middle	0.001	0.001	0.002	0.003	0.000	0.000	0.001	0.002	0.001	0.001	0.001	0.001
	Rear	0.000	0.001	0.001	0.002	0.000	0.000	0.001	0.001	0.000	0.001	0.001	0.002
σC_{my}	Head	0.064	0.065	0.068	0.081	0.001	0.001	0.034	0.029	0.055	0.070	0.066	0.058
	Middle	0.012	0.016	0.027	0.029	0.001	0.001	0.014	0.011	0.007	0.010	0.015	0.021
	Rear	0.036	0.042	0.040	0.034	0.003	0.004	0.013	0.025	0.029	0.037	0.031	0.033
σC_{mz}	Head	0.020	0.031	0.022	0.023	0.001	0.002	0.020	0.010	0.020	0.031	0.022	0.012
	Middle	0.015	0.020	0.030	0.025	0.001	0.003	0.012	0.009	0.013	0.016	0.013	0.009
	Rear	0.018	0.020	0.017	0.010	0.002	0.003	0.014	0.009	0.014	0.019	0.014	0.010

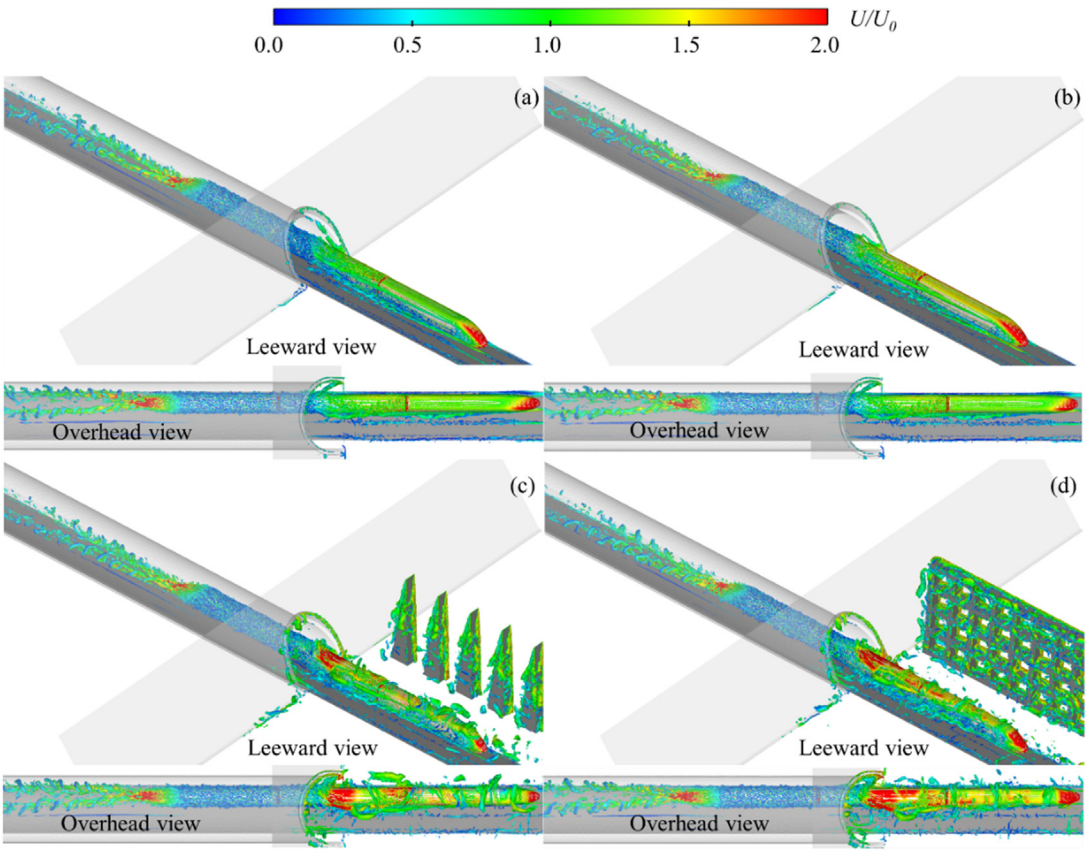

FIG. 16. The transient vortex structure when half of the HST leaves the tunnel: (a) C3, (b) C4, (c) C5, and (d) C6.

As shown in Fig. 16(a), two separate longitudinal vortex structures falloff either side of the rear carriage in the tunnel. As shown in Fig. 17(a), the HST wind interacts with the incoming flow, then the two elongated vortex structures (EVS) from which the rear carriage falls converge in the center of the HST and develop into a larger longitudinal vortex structure when the HST is running under the incoming flow. In further, a large longitudinal vortex structure shedding from the LWS of three carriages and two to three smaller longitudinal vortex structures shedding from the LWS of the head carriage can be observed. As the TKE decreased, the small EVS attached to the LWS of the middle and rear carriages gradually evolved into a small and dispersed small vortex structure. Finally, the vortex structure is dissipated and converted into heat. The area of high wind speed appears in the windscreen of the head carriage and the nose tip of the tail carriage, including the WWS and the connection of the HST. As shown in Figs. 17(a) and 17(b), as the incoming flow speed increases, the vortex structure detached from the LWS of the HST becomes more condensed and the vortex shedding distance is greater. The area of high wind speed at the head and rear of the HST's nose tip and the HST's WWS also gradually increases. Therefore, as the incoming flow speed increases, the vortex structure of the HST changes and the nonlinear aerodynamic force increases accordingly.

The TKE of the spire's LWS is higher, and the flow field change on the LWS is more disordered, especially at the tunnel entrance. A high intensity turbulent zone is formed at the tunnel entrance due to the interaction of the turbulent flow and the HST wind (as shown in Fig. 13). The local velocity at the WWS and the top of the carriage increases, and the longitudinal vortex structure with large shedding is often observed at the surface of the HST (Figs. 16 and 18). As a result, the peak nonlinear aerodynamic force of the HST at the tunnel entrance is higher than the incoming flow. When the HST is completely out of the tunnel, the vortex structure falling from the surface of the carriage develops into a separate vortex surround the HST surface. The number of vortex structures increases and they become scattered and disordered, showing obvious instability. As shown in Fig. 17, the trailing vortex of the HST changes from a longitudinal vortex structure to many discrete vortex formations.

The turbulent flow speed of the fence is higher than that of the spire. The interaction between the fence's turbulent flow and the HST wind is stronger, and the area of high wind speed on the HST surface is larger. There are more discrete vortex structures on the HST surface, resulting in a higher peak nonlinear aerodynamic force of the HST than the spire condition. As mentioned in Sec. IV A, the fence's turbulent flow has less turbulence intensity than the spire on the WWS.

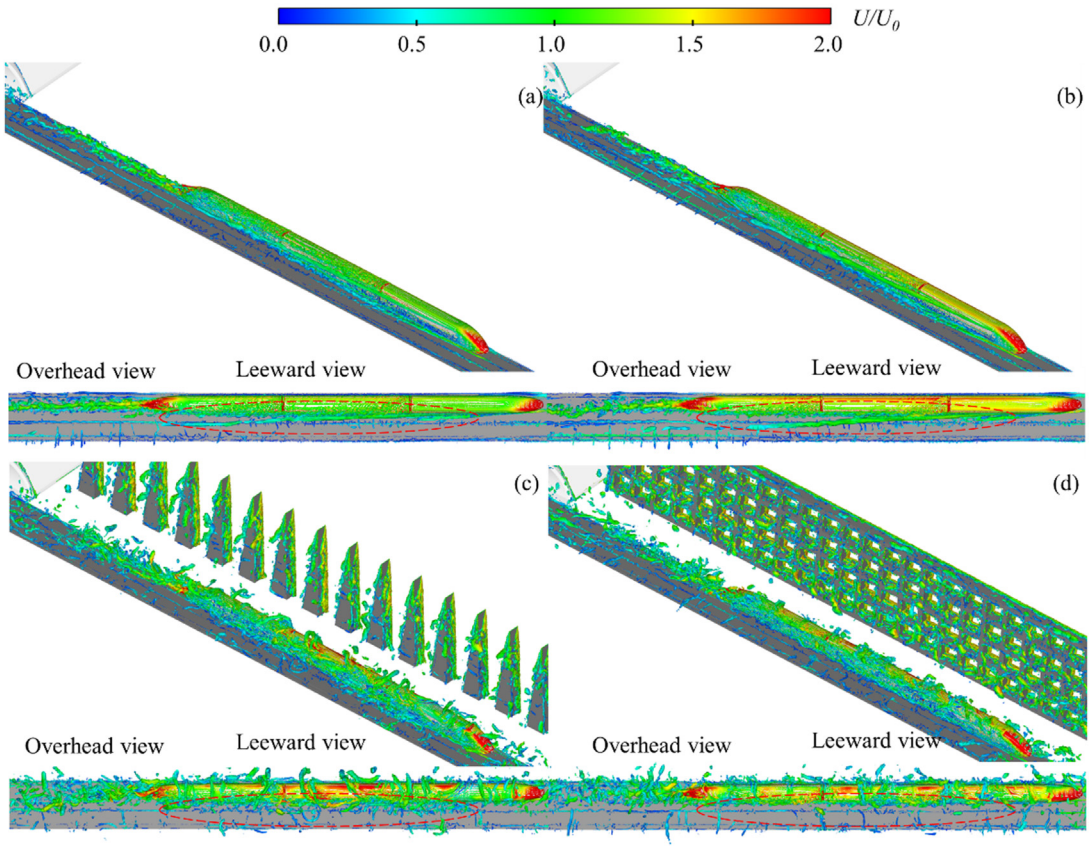

FIG. 17. The transient vortex structure when the HST runs completely in the crosswind environment: (a) C3, (b) C4, (c) C5, and (d) C6.

Therefore, as shown in Fig. 17, when the HST is completely out of the tunnel, the number of vortex structures falling around the carriage is less and the rate of fall is lower than that of the spire condition. In addition, the fluctuation range of the nonlinear aerodynamic force of the HST on the open line is smaller than in the spire condition.

3. PSD analysis

When the HST is away from the tunnel, the separation vortex and the longitudinal vortex structure will continue falling on the surface of the HST under the coupling effect of the incoming flow and the HST wind. These frequent shedding vortex structures directly aggravate the fluctuation of the nonlinear aerodynamic force of the HST. Therefore, PSD is introduced to further investigate the difference in the nonlinear aerodynamic force spectrum when the HST runs under the turbulent flow throughout the TFT process. Figure 19 shows the spectrum curve of the five nonlinear aerodynamic force coefficients of the head carriage.

Figure 19 shows the following:

(1) The overall trend of the PSD for each nonlinear aerodynamic force decreases with increasing frequency when the HST is operating under the incoming flow. Several main pneumatic frequency bands are concentrated in the 0–10 Hz range.
(2) In the low frequency band close to 0–1 Hz, under the turbulent flow of the spire and fence, the peak values of the PSD of the head carriage are lower than those of the corresponding incoming flow. This finding may indicate that the HST is under the incoming flow and the nonlinear aerodynamic force has maintained a large peak. However, under the turbulent flow of the spire and fence, the peak PSD value of the C_{mx} of the HST is 273 and 686 times the incoming flow of 11.50 m/s, and the rolling probability of the HST is greatly increased.
(3) Within the frequency of 1–10 Hz, the PSD curves of the five nonlinear aerodynamic force coefficients of the head carriage under the spire and fence are higher. This is because the nonlinear aerodynamic force of the HST fluctuates significantly under the effect of turbulent flow, and the HST swings and bounces up and down.

V. CONCLUSIONS

Based on the wind field tests at a typical TFT site and CFD simulations, the aerodynamic loads of the HST operating at the TFT site

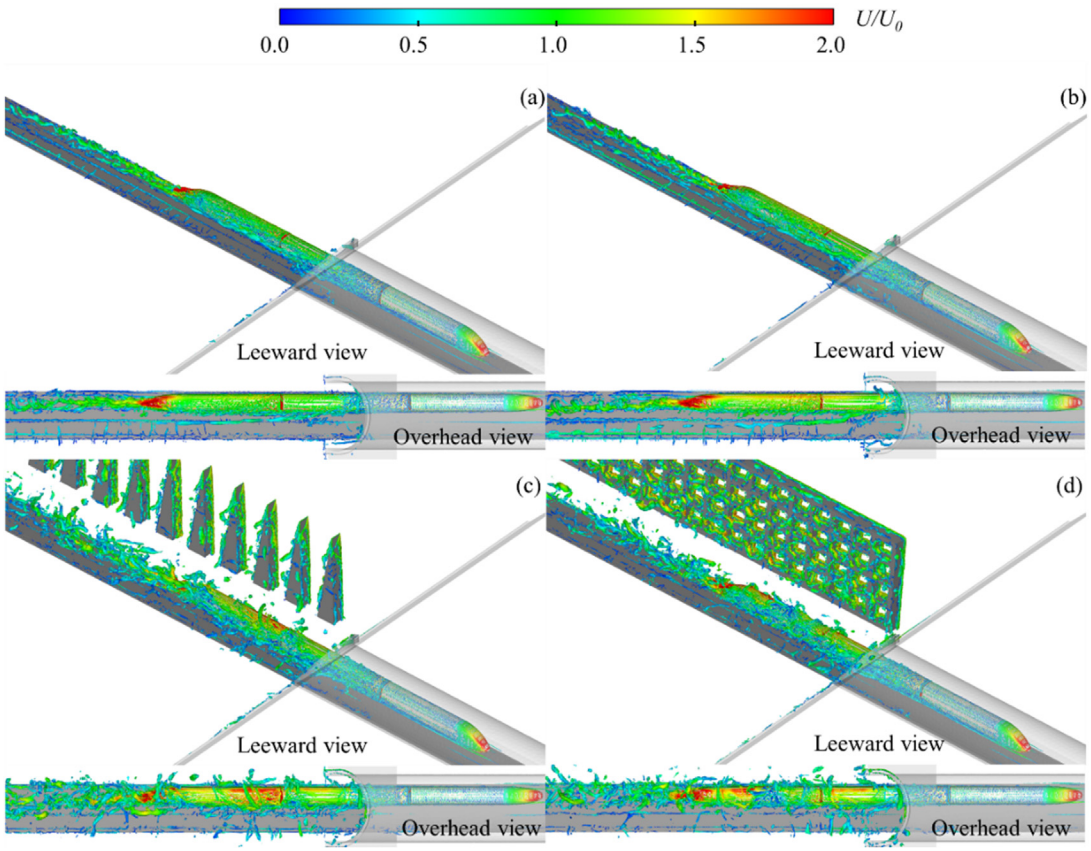

FIG. 18. The transient vortex structure when half of the HST enters the tunnel: (a) C3, (b) C4 and (c) C5, and (d) C6.

under incoming turbulent flow by two turbulence generators is discussed. The main conclusions are presented below:

(1) According to wind field tests, the measuring point for the high wind speed section of the TFT is usually between 9 and 14 m/s. The average wind direction of the high wind speed is 90° to the operating direction of the HST. The turbulence intensity tends to be 0.3 when the wind speed is more than 12 m/s.
(2) In the TFT scene, the turbulent flow generated by the spire is more similar to the measured characteristics. For the same blockage rate, the mean wind speed along the WWS and LWS is consistent with the measured peak wind speed range (0.5–0.7). In the Y direction, the turbulent flow of the spire is comparatively suitable for the wind speed profile.
(3) Under the turbulent flow of the fence, the peak of the nonlinear aerodynamic force coefficient when the HST leaves the tunnel is higher than that of the spire. However, when the HST is completely outside the tunnel, the fluctuation of the nonlinear aerodynamic force coefficient of the HST under the turbulent flow of the spire is more intense.
(4) According to the incoming flow of 11.50 m/s, the peak nonlinear aerodynamic load coefficients of the head carriage increase by 1.12–1.5 and 1.06–2.0 times, respectively, under the incoming turbulent flow generated by the spire and fence.
(5) The PSD peak values of the head carriage rolling moment coefficients at the spire and fence are 273 and 686 times the corresponding values for the incoming flow of 11.40 m/s. Within the frequency range of 1–10 Hz, the nonlinear aerodynamic forces of the head carriage at the spire and fence conditions fluctuate dramatically. The rolling probability of the HST increases significantly and the ride comfort decreases sharply.

The incoming turbulent flow generated by the spire is more consistent with the measured wind. Under the incoming turbulent flow generated by the spire, the study of the HST's aerodynamic load fluctuation law at tunnel entrance scenario provides a new method for vibration prevention and operation safety guarantee of the HSTs in future research.

This study mainly discusses the moving HST's nonlinear aerodynamic load under the spire and fence's turbulent flow. In future research, the wind-vehicle-flat ground-tunnel coupling dynamic model will be established. Future research aims to analyze the dynamic response of the train during operation and the possible safety risks under incoming turbulent flow generated by the turbulence generator. The aerodynamic loads of the HST under incoming turbulent flow are input into the wind-vehicle-flat ground-tunnel coupled dynamic model. Displacement and acceleration parameters, wheel-rail response, and travel safety indicators of the HST are obtained and analyzed.

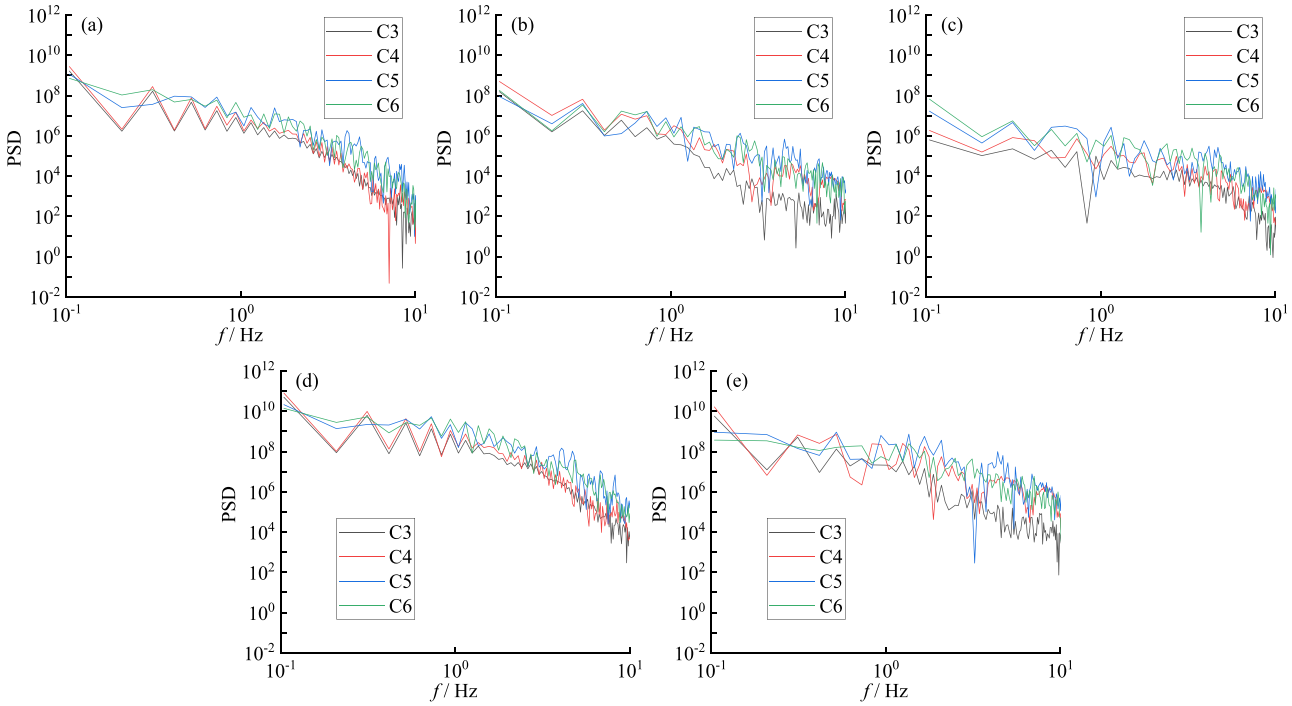

FIG. 19. PSD of the HST's aerodynamic coefficients: (a) C_z, (b) C_y, (c) C_{mx}, (d) C_{my}, and (e) C_{mz}.

ACKNOWLEDGMENTS

This work was funded by the National Natural Science Foundation of China (Grant No. 52308419), the Research Grants Council (RGC) of the Hong Kong Special Administrative Region (SAR) Government (Grant No. R-5020-18), the Innovation and Technology Commission of the Hong Kong SAR Government (Grant No. K-BBY1), and The Hong Kong Polytechnic University's Postdoc Matching Fund Scheme (Grant No. 1-W21Q).

AUTHOR DECLARATIONS

Conflict of Interest

The authors have no conflicts to disclose.

Author Contributions

Huan Yue: Data curation (lead); Investigation (lead); Software (lead); Writing – original draft (lead). **Jian Wang:** Data curation (equal); Software (equal); Validation (equal); Writing – review & editing (equal). **E Deng:** Conceptualization (lead); Data curation (equal); Funding acquisition (equal); Methodology (lead); Project administration (lead); Supervision (equal); Writing – review & editing (equal). **Yi-Qing Ni:** Funding acquisition (equal); Supervision (lead); Writing – review & editing (equal). **Weichao Yang:** Writing – review & editing (equal). **Xin-Yuan Liu:** Software (equal); Validation (equal); Writing – review & editing (equal). **Cheuk-Man Zeng:** Writing – review & editing (equal).

DATA AVAILABILITY

The data that support the findings of this study are available from the corresponding author upon reasonable request.

REFERENCES

[1]L. Shen, Y. Han, C. S. Cai, G. C. Dong, J. R. Zhang, and P. Hu, "LES of wind environments in urban residential areas based on an inflow turbulence generating approach," Wind Struct. **24**(1), 1–24 (2017).
[2]W. C. Yang, E. Deng, Z. H. Zhu, M. F. Lei, C. H. Shi, and H. He, "Sudden variation effect of aerodynamic loads and safety analysis of running trains when entering tunnel under crosswind," Appl. Sci. **10**(4), 1445 (2020).
[3]W. C. Yang, H. Yue, E. Deng, X. H. He, Y. F. Zou, and Y. W. Wang, "Comparison of aerodynamic performance of high-speed train driving on tunnel-bridge section under fluctuating winds based on three turbulence models," J. Wind Eng. Ind. Aerodyn. **228**, 105081 (2022).
[4]H. W. Xu, S. C. Yu, and W. J. Lou, "The loss coefficient for fluctuating flow through a dominant opening in a building," Wind Struct. **24**(1), 79–93 (2017).
[5]X. Z. Li, J. Xiao, D. J. Liu, M. Wang, and D. Y. Zhang, "An analytical model for the fluctuating wind velocity spectra of a moving vehicle," J. Wind Eng. Ind. Aerodyn. **164**, 34–43 (2017).
[6]J. Q. Niu, D. Zhou, and X. F. Liang, "Experimental research on the aerodynamic characteristics of a high-speed train under different turbulence conditions," Exp. Therm. Fluid Sci. **80**, 117–125 (2017).
[7]J. M. Olmosa and M. A. Astiz, "Improvement of the lateral dynamic response of a high pier viaduct under turbulent wind during the high-speed train travel," Eng. Struct **165**(15), 368–385 (2018).
[8]H. Kozmar and B. Laschka, "Wind-tunnel modeling of wind loads on structures using truncated vortex generators," J. Fluids Struct. **87**, 334–353 (2019).

[9]G. Chen, X. B. Li, and X. F. Liang, "IDDES simulation of the performance and wake dynamics of the wind turbines under different turbulent inflow conditions," Energy **238**, 121772 (2022).
[10]Y. P. Wang, Z. Y. Zhang, Q. W. Zhang, Z. Hu, and C. Q. Su, "Dynamic coupling analysis of the aerodynamic performance of a sedan passing by the bridge pylon in a crosswind," Appl. Math. Model. **89**, 1279–1293 (2021).
[11]Z. W. Chen, T. H. Liu, W. H. Li, Z. J. Guo, and Y. T. Xia, "Aerodynamic performance and dynamic behaviors of a train passing through an elongated hillock region beside a windbreak under crosswinds and corresponding flow mitigation measures," J. Wind Eng. Ind. Aerodyn. **208**, 104434 (2021).
[12]T. Li, M. G. Yu, J. Y. Zhang, and W. H. Zhang, "A fast equilibrium state approach to determine interaction between stochastic crosswinds and high-speed trains," J. Wind Eng. Ind. Aerodyn. **143**, 91–104 (2015).
[13]E. Deng, X. Y. Liu, Y. Q. Ni, Y. W. Wang, Z. W. Chen, and X. H. He, "Buffer scheme for aero-performance deterioration caused by trains passing bilateral vertical noise barriers with crosswinds," Eng. Appl. Comput. Fluid Mech. **17**(1), 2162585 (2023).
[14]F. Cheli, S. Giappino, L. Rosa, G. Tomasini, and M. Villani, "Experimental study on the aerodynamic forces on railway vehicles in presence of turbulence," J. Wind Eng. Ind. Aerodyn. **123**, 311–316 (2013).
[15]M. Bocciolone, F. Cheli, R. Corradi, S. Muggiasca, and G. Tomasini, "Crosswind action on rail vehicles: Wind tunnel experimental analyses," J. Wind Eng. Ind. Aerodyn. **96**(5), 584–610 (2008).
[16]Y. H. Noguchi, M. Suzuki, C. Baker, and K. Nakade, "Numerical and experimental study on the aerodynamic force coefficients of railway vehicles on an embankment in crosswind," J. Wind Eng. Ind. Aerodyn. **184**, 90–105 (2019).
[17]M. Masoud and A. R. Mohammad, "2D and 3D numerical and experimental analyses of the aerodynamic effects of air fences on a high-speed train," Wind Struct. **32**(6), 539–550 (2021).
[18]M. Masoud and A. R. Mohammad, "Multi objective optimization of aerodynamic design of high speed railway windbreaks using lattice Boltzmann method and wind tunnel test results," Int. J. Rail Transp. **6**(3), 183–201 (2018).
[19]M. L. Shur, P. R. Spalart, M. K. Strelets, and A. K. Travin, "A hybrid RANS-LES approach with delayed-DES and wall-modelled LES capabilities," Int. J. Heat Fluid Flow. **29**(6), 1638–1649 (2008).
[20]M. S. Gritskevich, A. V. Garbaruk, J. Schutze, and F. R. Menter, "Development of DDES and IDDES formulations to the k-ω shear stress transport model," Flow, Turbul. Combust. **88**, 431–449 (2012).
[21]J. Q. Niu, Y. C. Zhang, R. Li, Z. W. Chen, H. D. Yao, and Y. M. Wang, "Aerodynamic simulation of effects of one- and two-side windbreak walls on a moving train running on a double track railway line subjected to strong crosswind," J. Wind Eng. Ind. Aerodyn. **221**, 104912 (2022).
[22]W. C. Yang, H. Yue, E. Deng, Y. W. Wang, X. H. He, and Y. F. Zou, "Influence of the turbulence conditions of crosswind on the aerodynamic responses of the train when running at tunnel-bridge-tunnel," J. Wind Eng. Ind. Aerodyn. **229**, 105138 (2022).
[23]P. Tsoutsanis, I. W. Kokkinakis, L. Könözsy, D. Drikakis, R. J. R. Williams, and D. L. Youngs, "Comparison of structured- and unstructured-grid, compressible and incompressible methods using the vortex pairing problem," Comput. Methods Appl. Mech. Engrg. **293**, 207–231 (2015).
[24]B. J. R. Thornber and D. Drikakis, "Numerical dissipation of upwind schemes in low Mach flow," Numer. Methods Fluids **56**(8), 1535–1541 (2008).
[25]L. Wei, J. Zeng, H. Gao, and S. Qu, "On-board measuring of aerodynamic loads for high-speed trains negotiating transitions in windbreak walls," J. Wind Eng. Ind. Aerodyn. **222**, 104923 (2022).